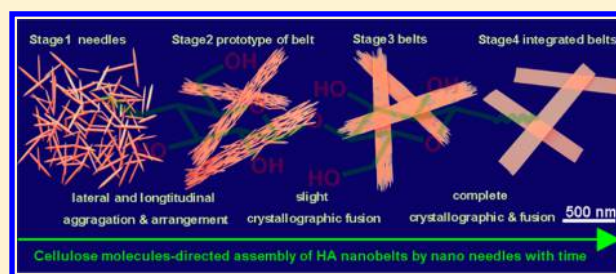


## Delicate Assembly of Ultrathin Hydroxyapatite Nanobelts with Nanoneedles Directed by Dissolved Cellulose

Xiaomin Ma,<sup>†,‡</sup> Wanjia Peng,<sup>‡,§</sup> Wen Su,<sup>†</sup> Zeng Yi,<sup>†</sup> Guangcan Chen,<sup>†</sup> Xiangyu Chen,<sup>†</sup> Bo Guo,<sup>\*,§</sup> and Xudong Li<sup>\*,†</sup><sup>†</sup>National Engineering Research Center for Biomaterials, Sichuan University, Chengdu 610064, P. R. China<sup>‡</sup>Institute of Advanced Synthesis, School of Chemistry and Molecular Engineering, Nanjing Tech University, Nanjing 211816, P. R. China<sup>§</sup>Department of Ophthalmology, West China Hospital, Sichuan University, Chengdu 610041, P. R. China

**ABSTRACT:** Living organisms make use of a variety of inorganic and organic components to form biogenic minerals with hierarchical structures and fascinating properties, triggering the development of biomimetic mineralization. The introduction of organic additive is a versatile strategy, and a wide range of organics have already been adopted to mimic biosystems designing and synthesizing advanced functional minerals. Insoluble cellulose is the most abundant polysaccharide in nature, but the insolubility has limited its extensive applications. In this study, we first find that concentrated calcium chloride aqueous solution is an effective solvent for cellulose, and dissolved cellulose plays a pivotal role in directing the formation of ultrathin hydroxyapatite (HA) nanobelts of ca. 10 nm in thickness. To investigate the assembling process of the belt, samples collected at different reaction times were observed. The results indicate that nanoneedles form first, and then they assemble into the prototype of nanobelts by lateral/longitudinal aggregation and arrangement. Subsequently, the nanobelts gradually become dense, transparent, and smooth via crystallographic fusion of adjacent nanoneedles, indicating the highly elaborated evolution of morphology resulted from a time-dependent process. During the evolution of nanobelts, dissolved cellulose is supposed to participate in the mineralization of HA via the bonding of its hydrophilic groups with phosphate groups and calcium ions and the interaction of cellulose molecules with HA crystal planes. These findings provide unique insight into the application of dissolved cellulose in aqueous solution and an inspiration of a bottom-up strategy for designing delicate mineral assemblies directed by insoluble organics.



## ■ INTRODUCTION

In nature, living organisms use various sources available to precisely fabricate hierarchically composite materials for the purposes of protection, mechanical support, and defense.<sup>1–3</sup> These materials generally possess a finely carved appearance and fascinatingly chemical and mechanical properties.<sup>4</sup> Calcium phosphate (CaP), as the main inorganic component of mammalian hard tissues, is a representative biomineral formed and spatially aligned between collagen fibrils.<sup>5</sup> Its sophisticated micro-/nanostructure and incomparably mechanical properties are superior to those of its synthesized counterparts. Thus, numerous efforts have been devoted to mimicking the biosystems to arrange ions and molecules into versatile CaP with exquisite architecture due to its widespread potential applications in various fields, including bone regeneration,<sup>6,7</sup> nonviral carriers for drug/gene delivery,<sup>8,9</sup> water treatment,<sup>10</sup> surface coating,<sup>11</sup> biomacromolecules immobilization,<sup>12,13</sup> vaccines protection,<sup>14</sup> diagnosis,<sup>15</sup> and so forth. The use of CaP in biomedical filed especially attracts much attention of the research community because of its excellent biocompatibility, biodegradability, and pH-responsive property. On account of these applications, the synthesis of CaP with different morphology, wide range of size, and hierarchical architecture

is of practical value and also a prerequisite. However, the control of CaP mineralization *in vitro* remains a challenge because the intrinsic pertinacious irregular agglomeration of CaP is hard to eliminate, and its morphology and size are readily affected by small changes of reaction condition.<sup>16</sup> Tailoring CaP to form assemblies with exquisite structure is even more challenging.

To obtain CaP with desirable characteristics and functions, various preparation methods have been developed, such as chemical precipitation,<sup>17,18</sup> hydrothermal reaction,<sup>19,20</sup> solid-state reaction,<sup>21</sup> sol–gel synthesis,<sup>22</sup> microemulsion,<sup>23</sup> microwave-assisted synthesis method,<sup>24</sup> electrodeposition techniques,<sup>25</sup> and so on. All of these methods have contributed to manipulating the manufacture of CaP with certain features and/or functions to some degree. For example, Ding et al. reported the preparation of yolk–shell porous microspheres of CaP by a microwave-assisted hydrothermal method. The obtained CaP spheres with high biocompatibility are pH-responsive and have relatively high protein/drug loading capacity and sustained protein/drug release.<sup>26</sup> Sui et al. reported the transformation of

Received: January 31, 2018

Published: April 3, 2018



calcium carbonate microparticles to CaP microparticles with high encapsulation efficiency for both high molecular weight and low molecular weight probes.<sup>27</sup> Santos et al. selected citrate as tailoring agents for the control of HA morphology. By altering the ratio of citrate/calcium, they achieved the assemblies of nanoscaled needlelike- and rodlike-shaped nanoparticles into larger microparticles with hedgehoglike or bundlelike aspects.<sup>28</sup>

Biomaterials are complex biocomposite materials with unique organic and inorganic components hierarchically organized with nano-/microscale precision. For example, enamel, a representative biogenic CaP, is the assembly of parallel arranged nanobundles directed by proteins, and this well-organized architecture contributes to its incomparable mechanical properties, mean Young's moduli of 87.5 ( $\pm 2.2$ ) and 72.7 ( $\pm 4.5$ ) GPa, and mean hardness of 3.9 ( $\pm 0.3$ ) and 3.8 ( $\pm 0.4$ ) GPa in directions parallel and perpendicular to the enamel rods, respectively.<sup>29</sup> Inspired and encouraged by the delicate natural biomaterials, the community attempted to improve the control of minerals facilitated by biomimetic strategy, which usually involves biomacromolecules, like collagen<sup>30,31</sup> and polysaccharides.<sup>32</sup> In addition, various acid proteins,<sup>33,34</sup> programmed peptides,<sup>35</sup> natural bioactive molecules,<sup>36</sup> and synthetic polymers<sup>37,38</sup> have been found to regulate the formation of minerals effectively, among which water-soluble additives can be used to alter polymorph selection through influencing the nucleation stage and also to modify the morphology of the crystals by interacting during the growth process.<sup>3</sup> Thus, natural water-soluble polysaccharides, such as chitosan,<sup>39</sup> hyaluronate,<sup>22</sup> alginate,<sup>19</sup> and modified cellulose<sup>40</sup> are exceptionally advantaged candidates because of their ease of obtaining biocompatibility, abundance in nature, and so on. In our previous work, alginate and hyaluronan have shown remarkable effects on regulating the morphology and size of CaP, directing the formation of HA nanorods and nanospheres, respectively.<sup>19,22</sup>

Cellulose constitutes the most abundant natural polysaccharide with the priorities of renewability, availability, nontoxicity, low-cost, environmental friendliness, biocompatibility, biodegradability, thermal and chemical stability, and derivatizability. Its molecular structure and typical shape are shown in Figure 1a,b, unbranched chains of glucose units linked head to tail, which form a hydrogen-bonded supramolecular structure.<sup>41</sup> Abundant hydrogen bonds lead to the insolubility of cellulose in water and most common organic liquids, which severely restricts its applications in many fields, even though its derivitized products have been applied in the paper, membrane,

fiber, polymer, and paints industries.<sup>42</sup> The growing willingness to develop cellulose-based materials results in the extensive research of solvents for cellulose. In 1934, Graenacher used molten N-ethylpyridinium chloride to successfully dissolve cellulose in the presence of nitrogen-containing bases.<sup>43</sup> Since then, various ionic liquids (ILs) have been developed to prepare cellulose solutions.<sup>44,45</sup> Swatoski et al. speculated that ILs containing concentrated  $\text{Cl}^-$  could be used as excellent candidates to dissolve cellulose fibers by breaking the hydrogen-bonding network.<sup>42</sup> In addition, nonderivatizing solvents of LiOH/urea and NaOH/urea aqueous solutions are reported to be able to break the intra- and intermolecular hydrogen bonds of cellulose, making cellulose soluble and applicable in aqueous solution.<sup>45</sup> The development of dissolution of cellulose has widened its application.<sup>46</sup>

Cellulose has been widely used for the synthesis of CaP. However, it is mostly used as a template for CaP, which can be attributed to its insolubility in water, and thus the formation of HA was actually the deposition of CaP upon insoluble cellulose objects. For example, HA-bacterial cellulose composite gels or scaffolds were achieved by alternate soaking of cellulose pellicle or scaffold in a calcium solution and phosphate solution.<sup>47,48</sup> Rodríguez et al. soaked electrospun cellulose-based scaffolds with varying treatments in simulated body fluid solution and investigated their bioactivity.<sup>49</sup> Cellulose grafted soy protein isolate was also reported to initiate rod-like HA through simulated body fluid.<sup>40</sup> Indeed, cellulose was used in the form of soluble molecules for the preparation of CaP. Salama et al. prepared cellulose/hydroxyapatite composites with highly ordered mesostructure by dispersing prefabricated HA nanoparticles into a solution of cellulose in [Bmim][Cl]. However, this method is complex, and the reaction is processed in ionic liquid at a relatively high temperature, which is not conformable to our aspiration of green and facile methods.<sup>50</sup>

Inspired by the ionic liquid containing high concentration of chloride, we selected concentrated calcium chloride aqueous solution as the dissolvent of cellulose and the provider of calcium ions for CaP. In this system, cellulose-tailored HA nanobelts were obtained by an ammonia diffusion method in aqueous solution at room temperature. The morphologic development of HA nanobelts was investigated by observing the precipitates at different times, and the nanobelts were found to be assembled by nanoneedles, which gradually integrated via crystallographic fusion between each other to evolve into uniform nanobelts. Dissolved cellulose is supposed to regulate the formation of nanoneedles and to direct the crystallographic assembly of nanoneedles into nanobelts here.

## EXPERIMENTAL SECTION

**Materials.** Cellulose (fibrous, medium) was purchased from Sigma-Aldrich. Calcium chloride ( $\text{CaCl}_2$ ), sodium phosphate monobasic dihydrate ( $\text{NaH}_2\text{PO}_4 \cdot 2\text{H}_2\text{O}$ ), and concentrated ammonia ( $\text{NH}_3 \cdot \text{H}_2\text{O}$ ) (25%, w/w%) were obtained from Kelong (Chengdu, China). All the reagents were analytical reagent grade. All the chemicals were used without further purification. Ultrapurified water ( $18.2 \text{ M}\Omega \cdot \text{cm}$ ) was used to prepare all the aqueous solutions.

**Methods. Dissolution and Regeneration of Cellulose.** Calcium chloride was selected as a substitute for ionic liquid here to dissolve cellulose. In a typical protocol, 88.0 g of calcium chloride, 1.0 g of cellulose powder, and 100 mL of ultrapurified water were added into a 250 mL flask under stirring, and then this feedstock solution was heated for 10 h at  $120^\circ\text{C}$  under reflux. After being cooled to room temperature, the cellulose solution was centrifuged ( $3000 \text{ g/min}$ , 10 min) to detach the undissolved fibers, and the supernatant was kept

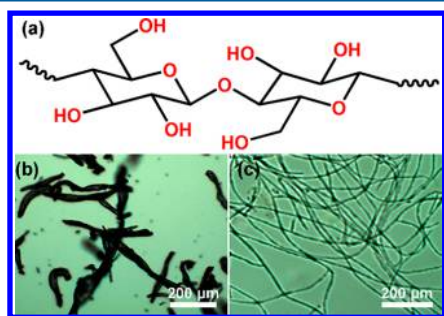


**Figure 1.** (a) Molecular structure and optical microscopy images of (b) crude and (c) regenerated cellulose. Hydrogen and oxygen atoms are shown in red.

for use. Regenerated cellulose could be visually observed by diluting the aforementioned cellulose aqueous solution to a tenth of the original volume by ultrapurified water (see Figure 1c). Regenerated cellulose precipitate was collected by centrifugation and rinsed with ultrapurified water. In the synthesis of CLHA, the freshly diluted cool solution of cellulose is used, which is supernatant with no precipitates.

**Synthesis of HA Nanobelts.** The precipitates of HA nanobelts regulated by cellulose (CLHA) were prepared by ammonia diffusion method. In each sample, the volumes of diluted cellulose solution (containing  $\text{CaCl}_2$ ),  $\text{NaH}_2\text{PO}_4 \cdot 2\text{H}_2\text{O}$  solution, and ultrapurified water were fixed at 2.5 mL, 2 mL, and 95.5 mL, respectively. (The ratio of Ca/P is 1.67.) Various reaction times, 6 h, 12 h, 36 h, and 72 h, were selected to investigate the morphologic evolution of the HA nanobelts. Thus, we designated the collected precipitates at different times as CLHA-6, CLHA-12, CLHA-36, and CLHA-72, respectively. In a typical procedure, a flask containing 100 mL solution with cellulose, calcium chloride, and sodium phosphate monobasic dihydrate and a flask of 100 mL concentrated ammonia were placed into a 2 L flask, which was sealed immediately with plastic film, and the reaction was initiated with the diffusion of  $\text{NH}_3$  from ammonia solution. After certain reaction times mentioned above, the pH values of the feedstock solutions are measured and recorded as 10.92, 10.78, 11.09, and 10.09 at 6 h, 12 h, 36 h, and 72 h, respectively. Then, HA nanobelts were separated from the reaction solutions by centrifugation at 10000 r/min for 10 min and rinsed with ultrapurified water thoroughly. After freeze-drying, the obtained precipitates were kept for further characterization. The control group of HA (CHA) was prepared with the same procedure as the CLHA samples but without cellulose, and the sample was collected after 6 h of reaction.

**Characterization of Samples.** To confirm the phase of CaP nanobelts, we conducted X-ray diffraction (XRD) measurements on a DX-1000 X-ray diffractometer with Cu  $K\alpha$  radiation ( $\lambda = 1.5406 \text{ \AA}$ ). The working voltage was 40 kV, and the working current was 25 mA. The data were collected at  $2\theta = 10\text{--}70^\circ$  at the scanning rate of  $0.06^\circ \text{ s}^{-1}$ . The molecular species of the nanobelts samples were determined by Fourier transform infrared spectroscopy (FT-IR) measurements with the KBr pellet method on a PerkinElmer Spectrum One B System. The spectra of the samples were recorded in the wavenumber range of  $4000\text{--}400 \text{ cm}^{-1}$  with the scanning resolution of  $2 \text{ cm}^{-1}$ . Scanning electron microscopy (SEM) images were taken with an S-4800 field emission scanning electron microscope (Hitachi, Japan) to observe the morphology and size of the samples. Atomic force microscope (AFM, Dimension Icom, Bruker) was adopted to characterize the surface features and thickness distribution of the nanobelts. Transmission electron microscopy (TEM) and high-resolution TEM (HR-TEM) images were examined with a Tecnai G<sup>2</sup> F20 STWIN transmission electron microscope to reveal the microstructural morphology and to confirm the crystallographic structure.

## RESULTS AND DISCUSSION

**Dissolution and Regeneration of Cellulose.** The morphology and size of cellulose were significantly altered after the dissolution–regeneration process. It is evident from Figure 1c that the long, much smaller fibers (fiber network) arose from the regeneration of cellulose dissolved from the diluted solution. According to SEM observation of collected sample after centrifugation, crude cellulose possesses the typical fibrous appearance seen in Figure 2a, and these pristine cellulosic macrofibrils have lengths of 25.2–282.2 and diameters of 9.2–27.0  $\mu\text{m}$ . In addition, the agglomeration of macrofibrils can be observed in Figure 2b, consistent with the reported results.<sup>51,52</sup> Then regenerated cellulose was obtained by diluting the cellulose solution. Visible regenerated cellulose gradually precipitated from the aqueous solution, which indicated that concentrated calcium chloride was an effective solvent for cellulose. The dissolution of cellulose is derived from the breaking of its intrinsic hydrogen bonds by

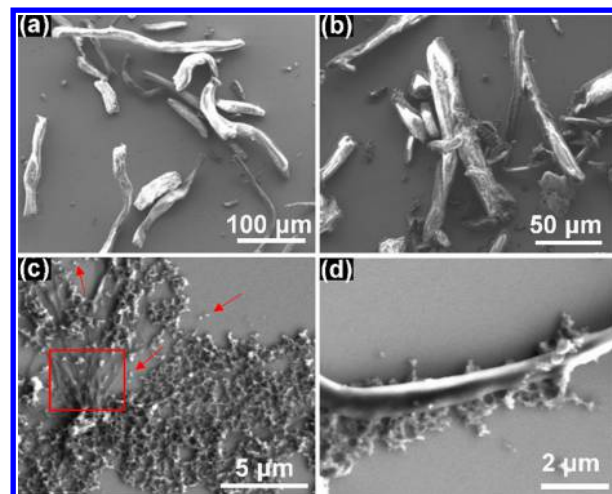
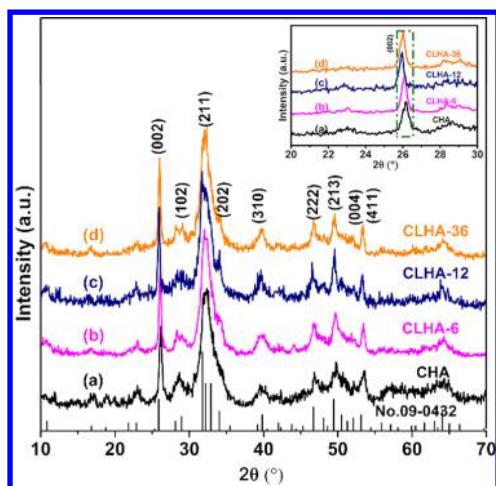


Figure 2. Morphology of (a, b) raw and (c, d) regenerated cellulose.

concentrated chloride ions. And once the concentration of chloride ions was decreased, hydrogen bonds gradually recovered, resulting in the precipitation of cellulose.<sup>42</sup> As shown in Figure 2c, most of the regenerated cellulose shows loosely porous network, consisting of numerous nanoparticles. Individual nanoparticles also exist separately indicated by arrows. Additionally, transparent cellulose fibers depicted with the square are observed in Figure 2c, with a diameter of less than 1  $\mu\text{m}$ , much smaller than the crude ones. Meanwhile, the coexistence of loosely porous network and fiber can also be seen in Figure 2d, and the fiber is denser, smoother, and much smaller in diameter than the crude ones. The SEM micrographs indicate that regenerated cellulose shows various existing forms at nano- and microscale compared with the macrofibrils of raw cellulose. Thus, concentrated calcium chloride solution is proved to be an effective and green solvent for cellulose. And this innovative approach may offer another choice for preparing regenerated cellulose with nanostructure.

**Crystal Phase and Molecular Structure of the Samples.** Calcium phosphates exist in different forms and phases depending on temperature, the presence of impurities, and partial pressure of water.<sup>53</sup> XRD was conducted to determine crystalline structure of the collected samples CHA, CLHA-6, CLHA-12, and CLHA-36 in this system. Figure 3 shows the XRD patterns of the obtained samples, and the standard diffraction data of HA is given as reference. It is evident that each sample possesses similar reflections, consistent with the standard data of JCPDS Card No. 09-0432 for crystalline HA, indicating the formation of HA rather than other calcium phosphate phases in this reaction system after all the selected reaction times. The representative reflections at  $2\theta = 26.0^\circ, 28.2^\circ, 32.0^\circ, 34.2^\circ, 39.8^\circ, 46.7^\circ, 49.6^\circ$ , and  $53.3^\circ$  can be attributed to (002), (102), (211), (202), (310), (222), (213), and (004)/(411) planes of HA, respectively. The broad feature reflections indicate that the synthetic products are poorly crystallized HA, which is generally associated with the wet chemistry of HA synthesis in ambient environment. However, a slight difference in the reflection attributable to (002) exists among HA precipitates in the presence and absence of cellulose. Compared with that of CHA (without using cellulose), this reflection shifts to a lower angle position in CLHA samples with the extended reaction times (the inset in Figure 3). This difference is due to the effect of cellulose on HA precipitation, suggesting the incorporation





**Figure 3.** XRD patterns of (a) CHA and CLHA nanobelts after different reaction times: (b) 6 h, (c) 12 h, and (d) 36 h. The inset is the XRD patterns in the range of 20–30°, indicating the shift of (002) resulted from cellulose.

of cellulose molecules in HA products. In fact, the similar crystallographic findings, e.g., change of the corresponding XRD reflections in both  $2\theta$  and intensity, were also reported in synthetic HA modulated with amino acids<sup>54</sup> and hyaluronan-mediated synthetic calcite crystals.<sup>55</sup> FT-IR spectra of crude cellulose and the collected CLHA-6, CLHA-12, CLHA-36, and CLHA-72 samples are also given in Figure 4 as the

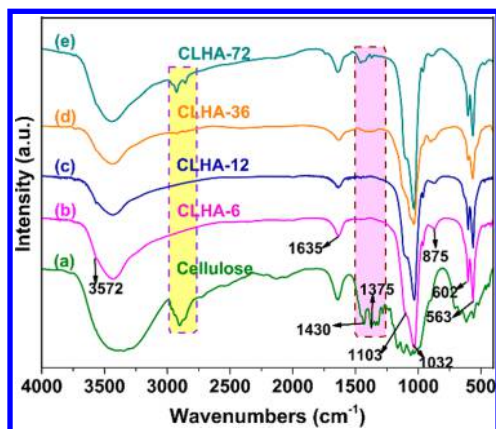


**Figure 4.** FT-IR spectra of (a) cellulose and CLHA nanobelts at different reaction times: (b) 6 h, (c) 12 h, (d) 36 h, and (e) 72 h.

supplemental evidence of molecular structure. In the spectra of CLHA samples, typical absorption peaks of HA are observed. The detectable peak at  $3572\text{ cm}^{-1}$  can be attributed to the stretching mode,  $\nu_s$ , of the hydroxyl group, and the peak at  $1635\text{ cm}^{-1}$  is assigned to associated water. The peak at  $1032\text{ cm}^{-1}$  is assigned to triply degenerated asymmetric stretching mode,  $\nu_{3c}$ , of the P–O bond of the phosphate group. The band at  $875\text{ cm}^{-1}$  is characteristic peak of hydrogen phosphate group and the peak at  $1103\text{ cm}^{-1}$  can be assigned to  $\text{HPO}_4^{2-}$  and/or  $\text{CO}_3^{2-}$ . And absorption bands at  $602$  and  $563\text{ cm}^{-1}$  are attributed to the triply degenerated bending mode,  $\nu_{4a}$  and  $\nu_{4c}$  of the O–P–O bonds of the phosphate group, respectively. The absence of the adsorption at  $631\text{ cm}^{-1}$  for OH of HA together with the broad adsorptions characteristic for phosphates of HA also indicates the low crystallinity of the products.<sup>31,56–58</sup> In addition, peaks of cellulose can also be

observed in CLHA sample. The HCH and OCH in-plane bending vibrations at  $1430\text{ cm}^{-1}$  and the CH deformation vibration at  $1375\text{ cm}^{-1}$  become gradually obvious with reaction times extending. Besides the specific peaks of cellulose, some of its bands overlap with the bands of HA at  $1635\text{ cm}^{-1}$  (the OH bending of adsorbed water),  $4000\text{--}2995\text{ cm}^{-1}$  (hydrogen-bonded OH stretching). Thus, FTIR spectra also indicate the inclusion of cellulose.<sup>59</sup>

**Morphologic Evolution of HA Nanobelts.** First, the control HA is observed by SEM in Figure 5. As previously

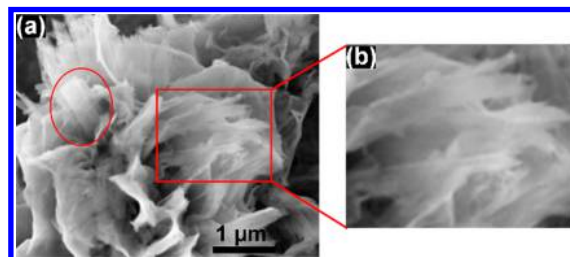


**Figure 5.** SEM images of (a) CHA and the magnification of the plate-like objects (b). Scale bar,  $1\text{ }\mu\text{m}$ .

reported,<sup>22</sup> the precipitates are irregular aggregates with a diameter of about  $5\text{ }\mu\text{m}$ . Thin plate-like objects forming flower-like agglomerates are the typical morphology of HA without any organic regulator. In addition, the appearance of thin belts can be seen marked with a circle. However, in the system with dissolved cellulose, an exquisite nanostructure of transparent nanobelts with a smooth surface was obtained. To investigate the formation process of the nanobelts, precipitates were collected at different reaction times, and their morphology was characterized by SEM seen in Figure 6. After ammonia diffusion for 6 h, the predominant form of HA is aggregated nanoneedles with a diameter of  $<27.8\text{ nm}$  in width and  $<295.6\text{ nm}$  in length. Meanwhile, a small number of prototypes of nanobelts (CLHA-6) have been observed shown in Figure 6a,b, which are assemblies of nanoneedles via parallel arrangement. In the magnified image of the marked areas (Figure 6c), incipient lateral/longitudinal aggregation and arrangement of several nanoneedles can be seen, which are supposed to be the initial stage of the assembly of nanoneedles into nanobelts. In this stage, loose aggregation between nanoneedles and obvious interspace between them in the nanobelt prototype result in the rough surface of the belts. When the reaction time is prolonged to 12 h, the majority of nanoneedles disappears and more nanobelts (CLHA-12) occur shown in Figure 6d,e, confirming the formation of nanobelt assemblies in the cost of consuming nanoneedles. Compared with CLHA-6 nanobelts, CLHA-12 nanobelt sample possesses denser structure, which may result from the crystallographic fusion of nanoneedles.<sup>36,60</sup> In Figure 6f, the imprint of nanoneedles gets faint but still discernible in/on belts due to the slight fusion of adjacent nanoneedles. However, the splintering of the nanobelts along the axis and also at the end of the belts in Figure 6f indicates that nanobelts in this stage are still unstable, and the crystallographic fusion between nanoneedles in CLHA-12 nanobelts remains to be further developed. Then continuing prolonging the reaction time, we got CLHA-36 nanobelts. The observed nanobelts (Figure 6g,h) are denser and more transparent than those of CLHA-12. The ambiguity of the individual nanoneedle as a building unit can be attributed to further crystallographic fusion of nanoneedles in nanobelts.<sup>60</sup> Even though the integration of

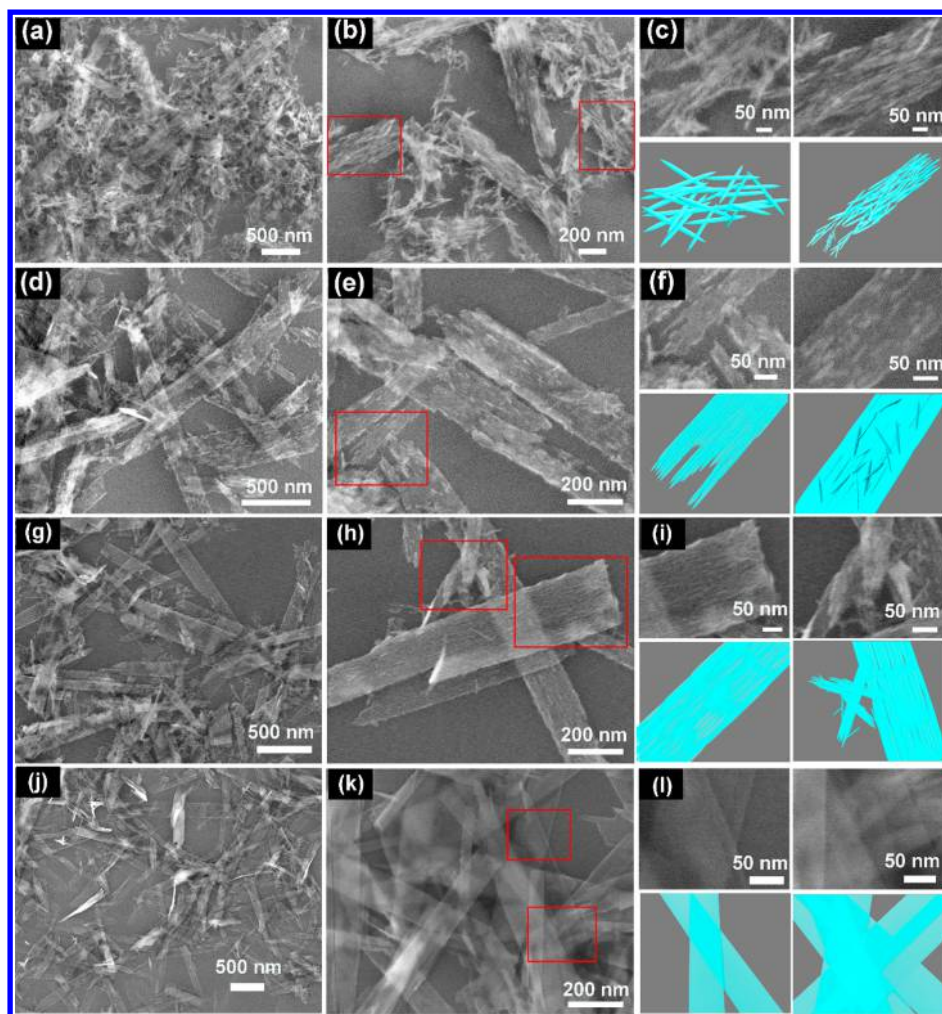


**Figure 6.** Morphologic evolution of HA nanobelts with time in the presence of cellulose, (a–c) 6 h; (d–f) 12 h; (g–i) 36 h; (j–l) 72 h. Scale bar are 500 nm (left column), 200 nm (middle column), and 50 nm (right column), respectively.

the nanoneedles has been well achieved to a large extent, uneven surface resulted from slight creases is clearly seen, and some small undeveloped belts still exist in Figure 6i. However, these defects are eliminated when the reaction time is extended to 72 h. In Figure 6j,k, definitely exquisite nanobelts can be observed, and there are no nanoneedles or any undeveloped nanobelts, indicating that the evolution of the morphology has got to a significantly advanced state. Each belt is an integrated entity, and the impression of the assembling pathway cannot be seen through at all because of the complete fusion of needles. According to Figure 6l, the overlap of several nanobelts is even discernible, indicating the belts are transparent and ultrathin. Thus, nanobelts of CLHA-72 show the most smooth and transparent features compared with the above samples. According to the above morphologic observation of different nanobelts, it can be concluded that the morphologic evolution of nanobelts is time-dependent. Characteristics of the nanobelts collected at different times have been summarized in Table 1.

**The Surface Development.** It has been characterized that the obtained HA nanobelts become dense and smooth with time. To further investigate this in detail, we conducted AFM measurements to quantify the surface topography of the nanobelts at 36 and 72 h, shown in Figure 7. The AFM images of CLHA-36 and CLHA-72 are remarkably different. In Figure 7a, the surface topography of CLHA-36 nanobelts is obviously

**Table 1.** Summary of the Characteristics of the Nanobelt Samples at Different Times

reaction time/h	morphologic information
6	nanoneedles (majority) prototype of belts (minority) with rough surface
12	loose nanobelts (majority) clear nanoneedle individual in/on the belts
36	dense and transparent nanobelts with slight crease
72	transparent integrated nanobelts with smooth surface

uneven, and there are several distinct linear areas along the axis of the nanobelt. The corresponding selective site cross-section (Figure 7b) indicates that the width of the nanobelt is ca. 300 nm with the fluctuant thickness distribution of the marked area. These two low-lying lines are supposed to be derived from the slight crease seen in Figure 6i. In contrast to CLHA-36, CLHA-72 shows a smooth surface, evidenced by the AFM image in Figure 7c,d. A partial uneven area in Figure 7c obviously results from the overlap of several nanobelts. The contrastive surface features of CLHA-36 and CLHA-72 reveal that the fusion and integration of nanoneedles are much better in CLHA-72 than those in CLHA-36, confirming the gradual development of HA nanobelt assemblies with time. It is worth noting that the thickness of the belts of CLHA-36 and CLHA-72 is similar,



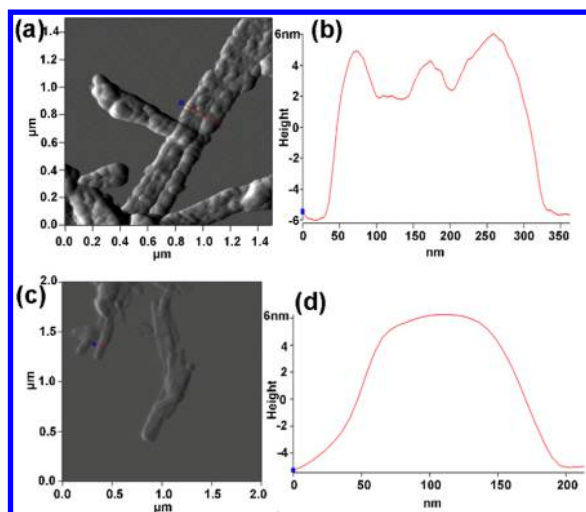


**Figure 7.** Surface topography and development of CLHA nanobelts with reaction times of 36 h (a, b) and 72 h (c, d).

about 10 nm, verifying the ultrathin property of nanobelts seen in SEM images in Figure 6.

**Microstructures of CLHA Belt.** TEM was adopted to observe the microstructure of CLHA-36 and CLHA-72 nanobelts. In Figure 8a, a heavy nanobelt with a size of 284

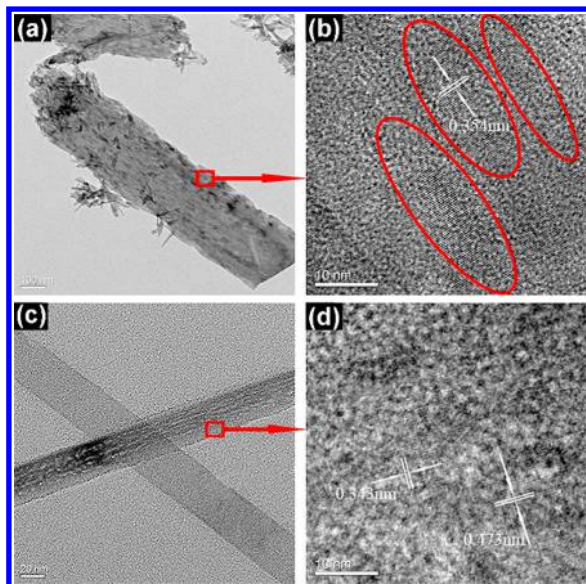


**Figure 8.** TEM and HR-TEM images of CLHA-36 (a, b) and CLHA-72 (c, d).

$\times 1,235$  nm is observed. Some nanoneedles are discernible in/on the belt due to the lack of fusion between needles. The needles at one end of the belt are especially clear, indicating the ongoing assembly of nanoneedles into belts at a given time and area. However, at the other end of this belt, the improved density and the lack of clear needles indicate the assembly process has almost finished in this area. In addition, some nanoneedles aggregate randomly at the border of the belt, while the needles in/on the belts are arranged orderly, suggesting that an ordered arrangement occurs after the initial aggregation. In the HR-TEM image shown in Figure 8b, fine crystal fringe with a interplanar spacing of 0.354 nm can be observed obviously, corresponding to the (002) plane of HA.<sup>19</sup> Three parallel

crystalline areas along the axial of the belt are circled. In CLHA-72 of 72 h, belts with a smoother surface are obtained as displayed in Figure 8c. Two thin and transparent belts are observed in the field of vision. One belt is smooth and exquisite, while the other one is comparably rough with a porous structure on the surface. There are several strands of pores located parallel in the belt. This saline feature is analogous to the AFM result of CLHA-36, showing this belt is still developing. From the image of HR-TEM in Figure 8d, discernible interplanar spacing of the fringes are measured, 0.343 and 0.473 nm, corresponding to the (002) and (110) planes of HA, respectively.<sup>19</sup>

**Possible Evolving Process of Nanobelts.** The above results have indicated that cellulose imposes an important effect on directing nanoneedles assembled into nanobelts. A possible morphologic evolution process of nanobelts is put forward as below in Figure 9. At the first stage, nanoneedles regulated by

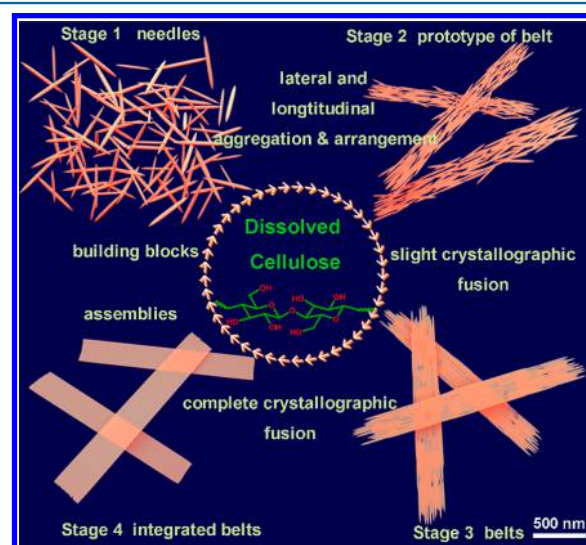


**Figure 9.** Possible formation process of CLHA nanobelts.

cellulose form and cellulose is supposed to participate in this process via bonding of its hydrophilic groups with phosphate groups and calcium ions.<sup>61</sup> Cellulose molecules, which are absorbed onto the surface and even incorporated, are supposed to play a pivotal role in directing the following assembly of HA nanobelts. In stage 2, cellulose molecules direct the nanoneedles to assemble into the prototype of nanobelts. This assembly is supposed to be organized by cellulose molecules via its steric hindrance, molecular recognition, hydrophilicity, and so on. Most of the nanoneedles here are consumed to form nanobelts, and the belts in this stage are severely rough and heavy. In stage 3, slight crystallographic fusion between nanoneedles occurs, leading to ambiguity of nanoneedles, while some slight creases are left because of the incomplete fusion. In this stage, nanobelts got comparably dense and transparent, but still unsatisfactory. In stage 4, the needles further crystallographically fuse with each other until adequate integration of nanoneedles occurs, and finally the most transparent and exquisite nanobelts have been achieved after enough reaction time. Most of present nanobelts are smooth, and each one is a uniform entity. And the development of nanobelts are thought to be finished here. During the development of CLHA nanobelts, cellulose molecules are pivotal in two processes: regulating the formation of nano-

needles like most other soluble organic additives via the interaction of its functional groups with calcium ions and phosphate groups and the adsorption of cellulose molecules on CaP crystal planes; directing the assembly of nanoneedles into nanobelts via its steric hindrance, molecular recognition, hydrophilicity, and so on.

## CONCLUSIONS

We innovatively selected calcium chloride aqueous solution as a substitute for ionic liquids to dissolve cellulose and as a provider of calcium ions for HA. The dissolved cellulose molecules played a directory role in the assembly of HA nanoneedles into nanobelts. Precipitates of HA nanobelts at different reaction times were collected to investigate the development of belts. Initially, the main form of precipitates is aggregated nanoneedles, and a small quantity of prototypes of nanobelts is discernible. With a longer reaction time, nanoneedles were consumed to assemble into rough and uneven nanobelts, which gradually became smooth and transparent via crystallographic fusion of nanoneedles. Finally, exquisite nanobelts were obtained after enough reaction time due to the complete integration of nanoneedles in the belts. The dissolved cellulose molecules are supposed to regulate the formation of nanoneedles via the interaction of hydrophilic groups with calcium ions and phosphate groups and to direct the assembly and integration of nanoneedles into nanobelts via its steric hindrance, molecular recognition, hydrophilicity, and so on. The present study offers a novel and green method to make use of cellulose as an organic modifier to regulate the mineralization and to direct the assembly of inorganic minerals in aqueous solution.

## AUTHOR INFORMATION

### Corresponding Authors

\*(B.G.) E-mail: [guobohx@163.com](mailto:guobohx@163.com).

\*(X.L.) Tel & Fax: +86 (0) 28 85412102 -mail: [xli20004@yahoo.com](mailto:xli20004@yahoo.com).

### ORCID

Xiaomin Ma: 0000-0003-3203-4507

Zeng Yi: 0000-0003-0473-2746

Xudong Li: 0000-0002-7939-5150

### Author Contributions

\*X.M. and W.P. contributed equally to this work.

### Notes

The authors declare no competing financial interest.

## ACKNOWLEDGMENTS

This work is supported by the National Natural Science Foundation of China (No. 51373106), the National Basic Research Program of China (No. 2012CB933600), the National Key Research and Development Program of China (No. 2016YFC1102700), and Sichuan Science and Technology Program Key Projects (No. 2017JY0018).

## REFERENCES

- (1) Lowenstam, H. A.; Weiner, S. *On Biomineralization*; Oxford University Press on Demand, 1989.
- (2) Stupp, S. I.; Mejicano, G. C.; Hanson, J. A. Organoapatites: Materials for Artificial Bone. II. Hardening Reactions and Properties. *J. Biomed. Mater. Res.* **1993**, *27*, 289–99.
- (3) Sommerdijk, N. A. J. M.; de With, G. Biomimetic CaCO<sub>3</sub> Mineralization Using Designer Molecules and Interfaces. *Chem. Rev.* **2008**, *108*, 4499–4550.
- (4) Sanchez, C.; Arribart, H.; Guille, M. M. G. Biomimetism and Bioinspiration as Tools for the Design of Innovative Materials and Systems. *Nat. Mater.* **2005**, *4*, 277–288.
- (5) Taton, T. A. Nanotechnology. Boning up on Biology. *Nature* **2001**, *412*, 491–2.
- (6) Pina, S.; Oliveira, J. M.; Reis, R. L. Natural-Based Nanocomposites for Bone Tissue Engineering and Regenerative Medicine: A Review. *Adv. Mater.* **2015**, *27*, 1143–1169.
- (7) Shi, F. N.; Almeida, J. C.; Helguero, L. A.; Fernandes, M. H.; Knowles, J. C.; Rocha, J. Calcium Phosphonate Frameworks for Treating Bone Tissue Disorders. *Inorg. Chem.* **2015**, *54*, 9929–35.
- (8) Kakizawa, Y.; Miyata, K.; Furukawa, S.; Kataoka, K. Size-Controlled Formation of a Calcium Phosphate-Based Organic-Inorganic Hybrid Vector for Gene Delivery Using Poly (Ethylene Glycol)-Block-Poly (Aspartic Acid). *Adv. Mater.* **2004**, *16*, 699–702.
- (9) Lee, M. S.; Lee, J. E.; Byun, E.; Kim, N. W.; Lee, K.; Lee, H.; Sim, S. J.; Lee, D. S.; Jeong, J. H. Target-Specific Delivery of siRNA by Stabilized Calcium Phosphate Nanoparticles Using Dopa-Hyaluronic Acid Conjugate. *J. Controlled Release* **2014**, *192*, 122–130.
- (10) Jiang, S. D.; Yao, Q. Z.; Zhou, G. T.; Fu, S. Q. Fabrication of Hydroxyapatite Hierarchical Hollow Microspheres and Potential Application in Water Treatment. *J. Phys. Chem. C* **2012**, *116*, 4484–4492.
- (11) Li, X.; Weng, J.; Tong, W.; Zuo, C.; Zhang, X.; Wang, P.; Liu, Z. Characterization of Hydroxyapatite Film with Mixed Interface by Ar<sup>+</sup> Ion Beam Enhanced Deposition. *Biomaterials* **1997**, *18*, 1487–1493.
- (12) Jung, S. W.; Byun, J. H.; Oh, S. H.; Kim, T. H.; Park, J. S.; Rho, G. J.; Lee, J. H. Multivalent Ion-Based in Situ Gelling Polysaccharide Hydrogel as an Injectable Bone Graft. *Carbohydr. Polym.* **2018**, *180*, 216–225.
- (13) Combes, C.; Rey, C. Adsorption of Proteins and Calcium Phosphate Materials Bioactivity. *Biomaterials* **2002**, *23*, 2817–23.
- (14) Wang, G. C.; Cao, R. Y.; Chen, R.; Mo, L. J.; Han, J. F.; Wang, X. Y.; Xu, X. R.; Jiang, T.; Deng, Y. Q.; Lyu, K.; Zhu, S. Y.; Qin, E. D.; Tang, R. K.; Qin, C. F. Rational Design of Thermostable Vaccines by Engineered Peptide-Induced Virus Self-Biomineralization under Physiological Conditions. *Proc. Natl. Acad. Sci. U. S. A.* **2013**, *110*, 7619–7624.
- (15) Deshmukh, K.; Shaik, M. M.; Ramanan, S. R.; Kowshik, M. Self-Activated Fluorescent Hydroxyapatite Nanoparticles: A Promising Agent for Bioimaging and Biolabeling. *ACS Biomater. Sci. Eng.* **2016**, *2*, 1257–1264.
- (16) Iijima, M.; Kamemizu, H.; Wakamatsu, N.; Goto, T.; Doi, Y.; Moriwaki, Y. Precipitation of Octacalcium Phosphate at 37° C and at Ph 7.4: In Relation to Enamel Formation. *J. Cryst. Growth* **1991**, *112*, 467–473.
- (17) He, L.; Deng, D.; Zhou, X.; Cheng, L.; ten Cate, J. M.; Li, J.; Li, X.; Crielard, W. Novel Tea Polyphenol-Modified Calcium Phosphate Nanoparticle and Its Remineralization Potential. *J. Biomed. Mater. Res., Part B* **2015**, *103*, 1525–1531.
- (18) Iannotti, V.; Adamiano, A.; Ausanio, G.; Lanotte, L.; Aquilanti, G.; Coey, J. M. D.; Lantieri, M.; Spina, G.; Fittipaldi, M.; Margaritis, G.; Trohidou, K.; Sprio, S.; Montesi, M.; Panseri, S.; Sandri, M.; Iafisco, M.; Tampieri, A. Fe-Doping-Induced Magnetism in Nano-Hydroxyapatites. *Inorg. Chem.* **2017**, *56*, 4446–4458.
- (19) Wang, Y. M.; Ren, X. X.; Ma, X. M.; Su, W.; Zhang, Y. P.; Sun, X. S.; Li, X. D. Alginate-Intervened Hydrothermal Synthesis of Hydroxyapatite Nanocrystals with Nanopores. *Cryst. Growth Des.* **2015**, *15*, 1949–1956.
- (20) Kim, T. G.; Park, B. Synthesis and Growth Mechanisms of One-Dimensional Strontium Hydroxyapatite Nanostructures. *Inorg. Chem.* **2005**, *44*, 9895–901.
- (21) Rao, R. R.; Roopa, H. N.; Kannan, T. S. Solid State Synthesis and Thermal Stability of Hap and Hap - Beta-Tcp Composite Ceramic Powders. *J. Mater. Sci.: Mater. Med.* **1997**, *8*, 511–8.



- (22) Chen, Z.; Zhou, H.; Wang, X.; Sang, L.; Wang, C.; Ma, J.; Li, X. Controlled Mineralization by Extracellular Matrix: Monodisperse, Colloidally Stable Calcium Phosphate-Hyaluronan Hybrid Nanospheres. *Chem. Commun.* **2010**, 46, 1278–80.
- (23) Shum, H. C.; Bandyopadhyay, A.; Bose, S.; Weitz, D. A. Double Emulsion Droplets as Microreactors for Synthesis of Mesoporous Hydroxyapatite. *Chem. Mater.* **2009**, 21, 5548–5555.
- (24) Qi, C.; Zhu, Y. J.; Chen, F.; Wu, J. Porous Microspheres of Magnesium Whitlockite and Amorphous Calcium Magnesium Phosphate: Microwave-Assisted Rapid Synthesis Using Creatine Phosphate, and Application in Drug Delivery. *J. Mater. Chem. B* **2015**, 3, 7775–7786.
- (25) Lin, K.; Wu, C.; Chang, J. Advances in Synthesis of Calcium Phosphate Crystals with Controlled Size and Shape. *Acta Biomater.* **2014**, 10, 4071–102.
- (26) Ding, G. J.; Zhu, Y. J.; Qi, C.; Sun, T. W.; Wu, J.; Chen, F. Yolk-Shell Porous Microspheres of Calcium Phosphate Prepared by Using Calcium L-Lactate and Adenosine 5'-Triphosphate Disodium Salt: Application in Protein/Drug Delivery. *Chem. - Eur. J.* **2015**, 21, 9868–76.
- (27) Sui, C.; Lu, Y.; Gao, H. L.; Dong, L.; Zhao, Y.; Ouali, L.; Benczedi, D.; Jerri, H.; Yu, S. H. Synthesis of Mesoporous Calcium Phosphate Microspheres by Chemical Transformation Process: Their Stability and Encapsulation of Carboxymethyl Chitosan. *Cryst. Growth Des.* **2013**, 13, 3201–3207.
- (28) Santos, C.; Almeida, M. M.; Costa, M. E. Morphological Evolution of Hydroxyapatite Particles in the Presence of Different Citrate:Calcium Ratios. *Cryst. Growth Des.* **2015**, 15, 4417–4426.
- (29) Habelitz, S.; Marshall, S. J.; Marshall, G. W., Jr.; Balooch, M. Mechanical Properties of Human Dental Enamel on the Nanometre Scale. *Arch. Oral Biol.* **2001**, 46, 173–83.
- (30) Nudelman, F.; Pieterse, K.; George, A.; Bomans, P. H.; Friedrich, H.; Brylka, L. J.; Hilbers, P. A.; de With, G.; Sommerdijk, N. A. The Role of Collagen in Bone Apatite Formation in the Presence of Hydroxyapatite Nucleation Inhibitors. *Nat. Mater.* **2010**, 9, 1004–9.
- (31) Wang, X.; Wang, X.; Ma, J.; Jiang, J.; Zheng, G.; Chen, Z.; Li, X. Versatile Nanostructured Processing Strategy for Bone Grafting Nanocomposites Based on Collagen Fibrillogenesis. *Adv. Appl. Ceram.* **2009**, 108, 384–388.
- (32) Fang, W. C.; Zhang, H.; Yin, J. W.; Yang, B. G.; Zhang, Y. B.; Li, J. J.; Yao, F. L. Hydroxyapatite Crystal Formation in the Presence of Polysaccharide. *Cryst. Growth Des.* **2016**, 16, 1247–1255.
- (33) He, G.; Dahl, T.; Veis, A.; George, A. Nucleation of Apatite Crystals in Vitro by Self-Assembled Dentin Matrix Protein 1. *Nat. Mater.* **2003**, 2, 552–8.
- (34) Ma, X.; Zhu, T.; Chen, Z.; Ma, J.; Zhang, Y.; Li, X. Gelatin Intervened Synthesis of Calcite Cocoon-Like Microparticles Assembled with Small Rhombohedra at Low Temperature. *Adv. Appl. Ceram.* **2016**, 115, 1–5.
- (35) Tsuji, T.; Onuma, K.; Yamamoto, A.; Iijima, M.; Shiba, K. Direct Transformation from Amorphous to Crystalline Calcium Phosphate Facilitated by Motif-Programmed Artificial Proteins. *Proc. Natl. Acad. Sci. U. S. A.* **2008**, 105, 16866–70.
- (36) Chen, Z. H.; Wang, C. H.; Zhou, H. H.; Sang, L.; Li, X. D. Modulation of Calcium Oxalate Crystallization by Commonly Consumed Green Tea. *CrystEngComm* **2010**, 12, 845–852.
- (37) Wada, N.; Horiuchi, N.; Nishio, M.; Nakamura, M.; Nozaki, K.; Nagai, A.; Hashimoto, K.; Yamashita, K. Crystallization of Calcium Phosphate in Agar Hydrogels in the Presence of Polyacrylic Acid under Double Diffusion Conditions. *Cryst. Growth Des.* **2017**, 17, 604–611.
- (38) Huang, X.; Andina, D.; Ge, J.; Labarre, A.; Leroux, J. C.; Castagner, B. Characterization of Calcium Phosphate Nanoparticles Based on a Pegylated Chelator for Gene Delivery. *ACS Appl. Mater. Interfaces* **2017**, 9, 10435–10445.
- (39) Luo, D.; Sang, L.; Wang, X.; Xu, S.; Li, X. Low Temperature, Ph-Triggered Synthesis of Collagen–Chitosan–Hydroxyapatite Nanocomposites as Potential Bone Grafting Substitutes. *Mater. Lett.* **2011**, 65, 2395–2397.
- (40) Salama, A.; Shukry, N.; El-Gendy, A.; El-Sakhawy, M. Bioactive Cellulose Grafted Soy Protein Isolate Towards Biomimetic Calcium Phosphate Mineralization. *Ind. Crops Prod.* **2017**, 95, 170–174.
- (41) Jarvis, M. Chemistry: Cellulose Stacks Up. *Nature* **2003**, 426, 611–2.
- (42) Swatloski, R. P.; Spear, S. K.; Holbrey, J. D.; Rogers, R. D. Dissolution of Cellulose [Correction of Cellose] with Ionic Liquids. *J. Am. Chem. Soc.* **2002**, 124, 4974–5.
- (43) Graenacher, C. Cellulose Solution. U.S. Patent, No. 1943176, 1934.
- (44) Huddleston, J. G.; Visser, A. E.; Reichert, W. M.; Willauer, H. D.; Broker, G. A.; Rogers, R. D. Characterization and Comparison of Hydrophilic and Hydrophobic Room Temperature Ionic Liquids Incorporating the Imidazolium Cation. *Green Chem.* **2001**, 3, 156–164.
- (45) Cai, J.; Zhang, L. Rapid Dissolution of Cellulose in Lioh/Urea and Naoh/Urea Aqueous Solutions. *Macromol. Biosci.* **2005**, 5, 539–48.
- (46) Zhu, S. D.; Wu, Y. X.; Chen, Q. M.; Yu, Z. N.; Wang, C. W.; Jin, S. W.; Ding, Y. G.; Wu, G. Dissolution of Cellulose with Ionic Liquids and Its Application: A Mini-Review. *Green Chem.* **2006**, 8, 325–327.
- (47) Favi, P. M.; Ospina, S. P.; Kachole, M.; Gao, M.; Atehortua, L.; Webster, T. J. Preparation and Characterization of Biodegradable Nano Hydroxyapatite–Bacterial Cellulose Composites with Well-Defined Honeycomb Pore Arrays for Bone Tissue Engineering Applications. *Cellulose* **2016**, 23, 1263–1282.
- (48) Hutchens, S. A.; Benson, R. S.; Evans, B. R.; O'Neill, H. M.; Rawn, C. J. Biomimetic Synthesis of Calcium-Deficient Hydroxyapatite in a Natural Hydrogel. *Biomaterials* **2006**, 27, 4661–4670.
- (49) Rodriguez, K.; Renneker, S.; Gatenholm, P. Biomimetic Calcium Phosphate Crystal Mineralization on Electrospun Cellulose-Based Scaffolds. *ACS Appl. Mater. Interfaces* **2011**, 3, 681–689.
- (50) Salama, A.; Neumann, M.; Gunter, C.; Taubert, A. Ionic Liquid-Assisted Formation of Cellulose/Calcium Phosphate Hybrid Materials. *Beilstein J. Nanotechnol.* **2014**, 5, 1553–68.
- (51) Liu, Z. H.; Sun, X. F.; Hao, M. Y.; Huang, C. Y.; Xue, Z. M.; Mu, T. C. Preparation and Characterization of Regenerated Cellulose from Ionic Liquid Using Different Methods. *Carbohydr. Polym.* **2015**, 117, 99–105.
- (52) Zhao, H. B.; Kwak, J. H.; Zhang, Z. C.; Brown, H. M.; Arey, B. W.; Holladay, J. E. Studying Cellulose Fiber Structure by Sem, Xrd, Nmr and Acid Hydrolysis. *Carbohydr. Polym.* **2007**, 68, 235–241.
- (53) Hench, L. L. Bioceramics, a Clinical Success. *Am. Ceram. Soc. Bull.* **1998**, 77, 67–74.
- (54) Matsumoto, T.; Uddin, M. H.; An, S. H.; Arakawa, K.; Taguchi, E.; Nakahira, A.; Okazaki, M. Modulation of Nanotube Formation in Apatite Single Crystal Via Organic Molecule Incorporation. *Mater. Chem. Phys.* **2011**, 128, 495–499.
- (55) Chen, Z.; Wang, C.; Zhou, H.; Li, X. Biomimetic Crystallization of Toplike Calcite Single Crystals with an Extensive (00.1) Face in the Presence of Sodium Hyaluronate. *Cryst. Growth Des.* **2010**, 10, 4722–4727.
- (56) Zhao, H.; Li, X.; Wang, J.; Qu, S.; Weng, J.; Zhang, X. Characterization of Peroxide Ions in Hydroxyapatite Lattice. *J. Biomed. Mater. Res.* **2000**, 52, 157.
- (57) Wang, X.; Wang, X.; Tan, Y.; Zhang, B.; Gu, Z.; Li, X. Synthesis and Evaluation of Collagen–Chitosan–Hydroxyapatite Nanocomposites for Bone Grafting. *J. Biomed. Mater. Res., Part A* **2009**, 89A, 1079–1087.
- (58) Elliott, J. C. Structure and Chemistry of the Apatites and Other Calcium Orthophosphates. *Stud. Inorg. Chem.* **1994**, 18, 213–234.
- (59) Oh, S. Y.; Yoo, D. I.; Shin, Y.; Seo, G. Ftir Analysis of Cellulose Treated with Sodium Hydroxide and Carbon Dioxide. *Carbohydr. Res.* **2005**, 340, 417–428.
- (60) Zhou, L.; O'Brien, P. Mesocrystals: A New Class of Solid Materials. *Small* **2008**, 4, 1566–1574.
- (61) Peacock, M. Calcium Metabolism in Health and Disease. *Clin. J. Am. Soc. Nephrol.* **2010**, 5, S23–S30.